Author Contributions:

Formal analysis: Utpal Saikia
Funding acquisition: Catherine A. Rychert, Nicholas Harmon
Project Administration: Catherine A. Rychert, Nicholas Harmon
Supervision: Catherine A. Rychert, Nicholas Harmon
Writing – original draft: Utpal Saikia
Writing – review & editing: Catherine A. Rychert, Nicholas Harmon, J. Michael Kendall

Seismic Attenuation at the Equatorial Mid-Atlantic Ridge Constrained by Local Rayleigh Wave Analysis From the PI-LAB Experiment

Utpal Saikia[1,2] , Catherine A. Rychert[1] , Nicholas Harmon[1] , and J. Michael Kendall[3]

[1]Ocean and Earth Science, University of Southampton, Southampton, UK, [2]Department of Earth and Climate Science, Indian Institute of Science Education and Research Tirupati, Tirupati, India, [3]Deparment of Earth Sciences, University of Oxford, Oxford, UK

Abstract The ocean lithosphere represents a simple realisation of the tectonic plate, offering a unique opportunity to better understand its physical and chemical properties in relationship to those of the underlying asthenosphere. While seismic velocity is frequently used to image the plate, seismic attenuation (Q_μ^{-1}) offers an important complimentary observation. We use fundamental mode Rayleigh waves from 17 local, $M > 4.2$ earthquakes recorded at stations located on 0–80 My old lithosphere near the equatorial Mid-Atlantic Ridge. We determine the attenuation coefficient (γ) for periods between 15 and 40 s and invert for 1-D average shear wave quality factor values (Q_μ) and shear wave velocity (Vs). We find Q_μ values of 175 ± 16 at 50 km depth, decreasing to 90 ± 15 at greater than 60 km. Comparison of our Q_μ and Vs measurements to previous observations from oceanic settings shows agreement in terms of higher Q_μ and Vs in the lithosphere in comparison to the asthenosphere. The observations from oceanic settings are in general agreement with the laboratory predictions for Q_μ-Vs relationships for thermal models. However, a small amount of partial melt (1%) is required to explain several previous observations. Our result also compares favorably to previous observations of lithospheric and asthenospheric attenuation with respect to frequency. Melt is not required for the 1-D average of our study area, consistent with previous electromagnetic and seismic imaging that suggested melt in punctuated and/or thin channel anomalies rather than over broad regions of the mantle.

Plain Language Summary Ocean plates cool and thicken with age following predictions for thermally defined lithosphere. However, many observations, for instance from seismic velocity imaging, are not consistent with thermal models and suggest greater complexity. The physical and chemical properties that define lithospheric plates are debated. Seismic attenuation, defined as the loss of energy of waves per cycle, provides complimentary constraints to seismic velocity because the two are predicted to vary with unique relationships depending on Earth properties. To date most oceanic seismic attenuation results are from the Pacific, which may be very different from the Atlantic. Here, we present a 1-D surface wave attenuation model for the lithosphere and the underlying asthenosphere at the equatorial Mid-Atlantic Ridge. We find general agreement with previous global and regional observations that find lower attenuation and higher shear wave velocity in the lithosphere in comparison to the asthenosphere. Comparison to laboratory predictions indicates that temperature can explain some of the global observations. Partial melt is required to explain the full range of asthenospheric observations. Our 1-D average result can be explained by a thermal model and does not require partial melt. The result likely reflects variability in the presence/absence of melt across the region.

1. Introduction

Determining the physical and chemical properties of the lithosphere and the asthenosphere is crucial for a better understanding of plate tectonics. Most of the Earth's tectonic plates are comprised of oceanic lithosphere, which is thought to have a relatively simple tectonic history and composition. The relative simplicity of the oceanic upper mantle makes it the ideal place for studying the lithosphere-asthenosphere system. Simple thermal models such as half space cooling or plate cooling are effective at explaining a substantial amount of the geophysical observations in the oceans (Dalton et al., 2014; Parsons & Sclater, 1977; Stein & Stein, 1992) and the composition of the mantle is well constrained from the volcanic outputs at mid-ocean ridges (Klein & Langmuir, 1987). Mid-ocean ridges are also particularly important for our understanding of the plate given that this is where the plate is formed from the upwelling of asthenospheric mantle (Forsyth, 1992; Forsyth et al., 1998; Nishimura &

Forsyth, 1988). The lithosphere then cools and thickens with age as inferred from observations of a thickening seismically fast lid underlain by lower velocities (Harmon et al., 2009; Kawakatsu et al., 2009; Nettles & Dziewoński, 2008; Nishimura & Forsyth, 1988; Priestley & McKenzie, 2013; Ritzwoller et al., 2004).

Generally most studies find a slow shear wave (Vs) and compressional (Vp) velocity, low resistivity, and high shear wave attenuation (Q_μ^{-1}) zone directly beneath mid-oceanic ridges in the asthenosphere (Eilon & Abers, 2017; Evans et al., 2005; Johansen et al., 2019; Key et al., 2013; Nishimura & Forsyth, 1989; Shapiro & Ritzwoller, 2002). There has been a long debate about the causes of such anomalies beneath the ridge areas, in other words whether it is owing to high temperatures that occur in response to passive upwelling and/or buoyant and active upwelling or whether other factors are required. In general seismic velocities, resistivities, and quality factors (inverse attenuation values , Q_μ) beneath ridges are too low to be explained by thermal processes alone (Eilon & Abers, 2017; Forsyth et al., 1998; Harmon et al., 2020; Johansen et al., 2019; Key et al., 2013; Saikia et al., 2021; Wang et al., 2020).

In addition, the definition of the plate as it evolves is debated, in other words, whether the plate is thermally defined at older ages or another factor distinguishes the lithosphere from the asthenosphere. Seismic studies of older oceanic lithosphere that include underside reflections suggest a discontinuity at relatively constant depth, ∼60 km, that is also relatively sharp (typically occurring over <30 km), which is not well-explained by the half-space cooling model (Gaherty et al., 1996; Rychert & Shearer, 2011; Schmerr, 2012; Tan & Helmberger, 2007; Tharimena et al., 2017). A number of receiver functions (RFs) studies also find a strong, sharp discontinuity beneath the oceanic plates (Akuhara et al., 2021; Hannemann et al., 2017; Kawakatsu et al., 2009; Kumar & Kawakatsu, 2011; Mark et al., 2021; Reeves et al., 2015; Rychert & Shearer, 2011; Rychert et al., 2018a, 2018b, 2021; Schmerr, 2012; Tonegawa et al., 2019; Zhang & Olugboji, 2021). Active source imaging find unexpected sharp discontinuities associated with channels (Mehouachi & Singh, 2018; Qin et al., 2020; Stern et al., 2015). Magnetotelluric imaging also finds a low resistivity channels that are also not explained by thermal models (Naif et al., 2013).

A host of sub-solidus conditions have been proposed to explain the low velocities, low resistivities, low Q_μ and discontinuities at constant depth across variably aged lithosphere, and/or sharp discontinuities. These include grain size (Jackson & Faul, 2010), elastically accommodated grain boundary sliding owing to hydration (Karato & Park, 2019), enhanced effects of near melt conditions on seismic waves (Yamauchi & Takei, 2016), a change in anisotropy (Auer et al., 2014; Beghein et al., 2014; Burgos et al., 2020), and the oxidation state of the mantle (Cline et al., 2018). However, none of these possibilities explain all of observations with a range of sensitivities. Partial melt provides an attractive option, given that it is predicted to have a large influence on seismic waves and also magnetotelluric imaging (Clark & Lesher, 2017; Hammond & Humphreys, 2000; Ni et al., 2011) However, geochemical constraints (Albarède, 1998; Gale et al., 2013) and also theoretical permeability models suggest that melt should not persist in the mantle over time and length scales that would be seismically imageable (Mckenzie & Bickle, 1988; Turner & Hawkesworth, 1997). Therefore, the debate continues.

One challenge in determining the factors that explain the observations is that they are often from different methods with different sensitivities in different locations, and most observations are of seismic velocity. Q_μ^{-1} observations are particularly valuable because they provide complementary sensitivity to the more commonly constrained seismic velocity, providing additional insight, especially when combined with velocity. Experimental studies suggest that Vs and Q_μ^{-1} should have a unique relationship with increasing Q_μ^{-1} and decreasing Vs as temperature increases (Havlin et al., 2021; Jackson & Faul, 2010; McCarthy et al., 2011; Yamauchi & Takei, 2016). This relationship is also likely different for other parameters such as variable grain size, hydration, or partial melt (Havlin et al., 2021; Jackson & Faul, 2010; Karato & Park, 2019; McCarthy et al., 2011; Yamauchi & Takei, 2016).

Experimental constraints also suggest that the frequency dependence of Q_μ^{-1} may be different in the lithosphere in comparison to the asthenosphere possibly because of different properties such as the presence of partial melt (Faul et al., 2004; Jackson & Faul, 2010) or hydration (Karato & Park, 2019). Different frequency dependencies of Q_μ^{-1} in the lithosphere and the asthenosphere have been observed by oceanic Q_μ^{-1} studies using waveforms at different periods beneath very old (>100 Myr) Pacific seafloor and interpreted in terms of either partial melt and/or pre-melt conditions (Takeuchi et al., 2017; Yamauchi & Takei, 2016). Less variability in frequency dependence has also been suggested beneath 70 Myr old Pacific lithosphere (Ma et al., 2020).

At a global scale, surface wave imaging finds low Q_μ beneath most of the Earth's ridges and rifts and high Q_μ beneath the ancient stable continental interiors, likely reflecting first order variations, such as higher and lower temperatures, respectively (Dalton et al., 2008). Global surface wave attenuation studies also distinguish high Q_μ lithospheric lids overlying low Q_μ asthenosphere beneath the oceans (Dalton et al., 2008). Attenuation anomaly observations in subduction zone mantle wedges have also been used to infer the locations of thermal anomalies, water, and partial melt (Eberhart Phillips et al., 2013, 2020; Ko et al., 2012; Myers et al., 1998; Pozgay et al., 2009; Schurr et al., 2003; Stachnik et al., 2004; Takanami et al., 2000; Tsumura et al., 2000). The complimentary sensitivities of attenuation and velocity have also been used to further distinguish the locations and pathways of water and melt through the mantle wedge (Rychert et al., 2008; Syracuse et al., 2008; Wei et al., 2015; Wei & Wiens, 2018).

Consideration of Vs and Q_μ observations together in oceanic settings is also particularly helpful in constraining the properties of the Earth. So far there have been a handful of high resolution in situ studies of Q_μ, several of which also constrain Vs, and these have been primarily from the Pacific. Beneath young seafloor age (<10 Myr) at the ultra-fast spreading East Pacific Rise (EPR) at 17°S a study using Rayleigh waves and the two plane wave method and a minimum parameterization, found $Q_\mu = 184 \pm 20$ and Vs $= 4.27 \pm 0.05$ km/s for the lithosphere and $Q_\mu = 79$–98 and Vs $= 4.11 \pm 0.06$ km/s for the asthenosphere (Yang et al., 2007). A study using the same method and a minimum parameterization on similar aged seafloor at the intermediate, but hotspot influenced Juan de Fuca Ridge found $Q_\mu = 114 \pm 40$ and Vs $= 4.29 \pm 0.06$ km/s in the lithosphere and $Q_\mu = 46 \pm 6$ and Vs $= 4.23 \pm 0.03$ km/s in the asthenosphere (Ruan et al., 2018). A higher frequency study using body waves in the same region found $Q_\mu = 25$ near the ridge and $Q_\mu < 90$ away from the ridge in the region (Eilon & Abers, 2017). A study on older seafloor, near the NoMelt experiment on 70 Myr old seafloor using Rayleigh waves found $Q_\mu = 1,400 \pm 14$ and Vs $= 4.54 \pm 0.09$ km/s in the lithosphere and $Q_\mu = 110 \pm 16$ and Vs $= 4.28 \pm 0.05$ km/s in the asthenosphere (Ma et al., 2020). Finally, at high frequency on very old lithosphere >100 Myr old using Po/So, Takeuchi et al. (2017) found $Q_\mu = 3,200$ in the lithosphere and $Q_\mu = 60$ the asthenosphere.

These studies from the Pacific have greatly increased our understanding of the plate, yet ocean bottom seismic deployments in the Atlantic have been relatively rare. The Mid-Atlantic Ridge is characterized by slow spreading (~2 mm/year half-spreading rate), much slower than the ultra-fast spreading EPR (~16–18 mm/year half spreading rate). Different spreading rates are predicted to result in variations in associated dynamics and ridge processes (Parmentier & Morgan, 1990), with important implications for the formation and evolution of the lithosphere-asthenosphere system. Additional measurements of attenuation at a broad range of frequencies and from different aged lithosphere formed at different spreading rates are required to settle long-held debates regarding the nature of the lithosphere-asthenosphere system (e.g., Abers et al., 2014; Artemieva, 2006; Auer et al., 2014; Beghein et al., 2014; Burgos et al., 2020; Cline et al., 2018; Eaton et al., 2009; Faul & Jackson, 2005; Fischer et al., 2020; Ford et al., 2010; Gaherty et al., 1996; Holtzman et al., 2003; Karato & Park, 2019; Kawakatsu et al., 2009; Priestley & McKenzie, 2013; Rychert et al., 2007; Rychert et al., 2010; Rychert et al., 2020; Rychert & Shearer, 2009; Sarafian et al., 2015; Stern et al., 2015; Yamauchi & Takei, 2016).

Here, we present results from the Passive Imaging of the Lithosphere Asthenosphere Boundary (PI-LAB) experiment and the Experiment to Unearth the Rheological Oceanic Lithosphere-Asthenosphere Boundary (EURO-LAB) at the equatorial Mid Atlantic (Harmon et al., 2018, 2020, Harmon, Rychert, et al., 2021; Agius et al., 2018, 2021; Bogiatzis et al., 2020; Hicks et al., 2020; Leptokaropoulos et al., 2021; Rychert et al., 2021; Saikia et al., 2020, 2021; Wang et al., 2020), which was designed to image the base of the tectonic plate and determine what makes a plate, plate-like (Rychert et al., 2005, 2016, 2018a, 2018b; Rychert & Shearer, 2009). In this study, we image the upper mantle Q_μ^{-1} beneath the equatorial Mid-Atlantic Ridge. First, we measure the attenuation coefficient (γ) parameter at the period range 15–40 s using Rayleigh wave amplitude data from surface waves. Then the attenuation coefficients are inverted to determine a 1-D Q_μ model for the study region as a function of depth. We compare our Q_μ result to previous Q_μ and Vs studies of oceanic lithosphere and laboratory predictions to determine the physical state of upper mantle in our study area. We also compare our results to previous observations to determine the frequency dependence of Q_μ^{-1} in the lithosphere and the asthenosphere.
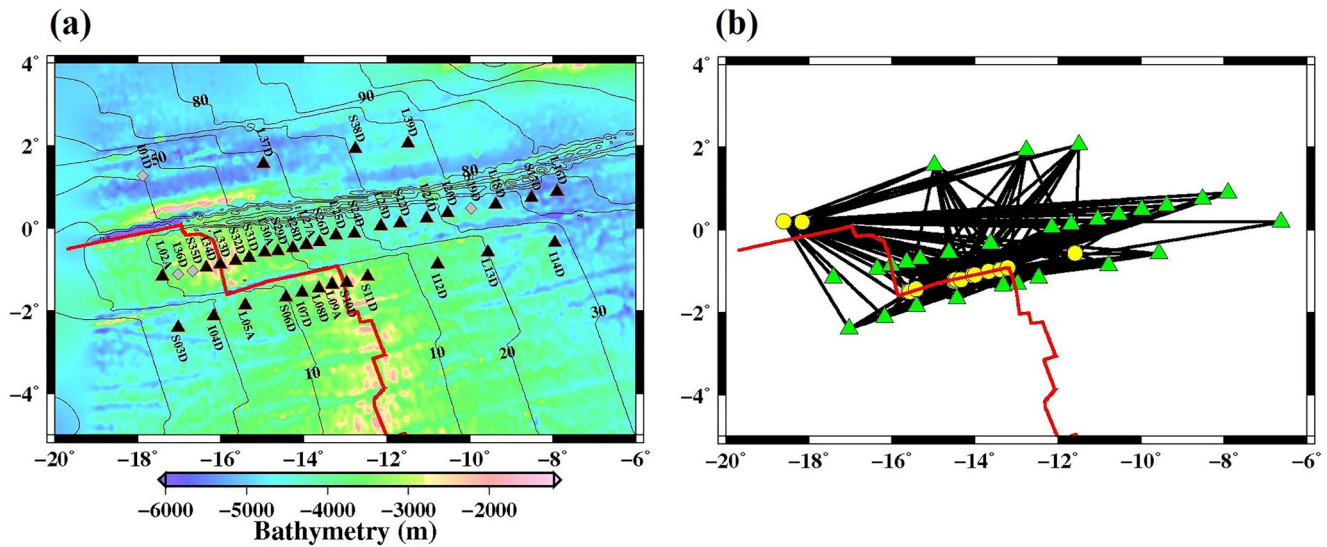
Figure 1. Map of the study area and data ray paths.(a) The bathymetry of the study region along with the locations of seismic stations used in the study (black triangles) and the seismic stations not used in the study (gray triangles) are shown. The thin black contours indicate the ages of the seafloor. (b) Ray paths (black lines) between the local events used in the study (yellow circles; magnitude > 4.2) andthe seismic stations used in the study (green triangles) for data analysis are shown. The Mid-Atlantic Ridge plate boundary is shown as the thick red line in both panels.

2. Data and Methodology

We use data from the PI-LAB experiment, which includes 39, 3-component broadband Ocean Bottom Seismometers (OBS) each equipped with a differential pressure gauge (DPG), which was deployed from March 2016 to March 2017 (Figure 1). We use vertical component Rayleigh wave seismograms for local earthquake events. We use 17 events having magnitudes greater than or equal to 4.2 (black stars in Figure 1). Although initially 39 stations were installed, two stations (I01D and I36D) were not recovered, and 2 stations had technical errors caused by a lack of recording of one or more channels. Some station records also exhibit tilt caused by strong motion in the near-field and are excluded from the analysis. The ray-paths and stations are shown in Figure 1. Example waveforms for two events are shown in Figure 2.

We use surface wave amplitude to estimate the attenuation coefficient in the period range of 15–40 s. In general, the surface wave attenuation can be described by $e^{-\gamma r}$, where γ is the attenuation coefficient and r is distance, which is related to surface wave quality factor (Q) as $Q = \pi f / U \gamma$, where U is the group velocity and f is frequency. The attenuation coefficient is estimated from the frequency domain seismogram, $S(f)$ using the following formula:

$$|S(f)| = A(f)|H_0(2\pi f r/C(f))|e^{-\gamma r}(cos(2[\theta - \varphi])) \tag{1}$$

where A is the amplitude of the event at a given frequency, H_0 is the zero order Hankel function for frequency f, and C represents the phase velocity. The $cos(2[\theta - \varphi])$ term of back azimuth θ and apparent earthquake radiation direction φ, account for the source radiation pattern of each earthquake at each period (Mitchell, 1995). We choose the Hankel function because our study is at a near-to-intermediate distance range of the earthquakes, and we cannot use the asymptotic plane wave approximation to match the amplitude. The Hankel function precisely captures the geometric spreading of surface waves, with its complex sinusoidally decaying amplitude with distance. Observe amplitude variations as a function of distance for two events is shown in Figure 3. We use the 1-D phase velocities for the region estimated from the vertical component Rayleigh wave observations of teleseismic events and ambient noise in this period range (Harmon et al., 2020). The phase velocities at <18 s are not reported by Harmon et al. (2020) although they are consistent with the group velocity measurements reported by Saikia et al. (2021). Here, we show the average phase velocity variations at the period range of 15–111 s in Figure 4c. We use a grid search method to determine the amplitude (A) of the source spectra at the given frequency and the attenuation coefficient. We use a grid spacing 200 in A from 1,000 to 10,000 and γ from 0 to 7.5×10^{-4} with a
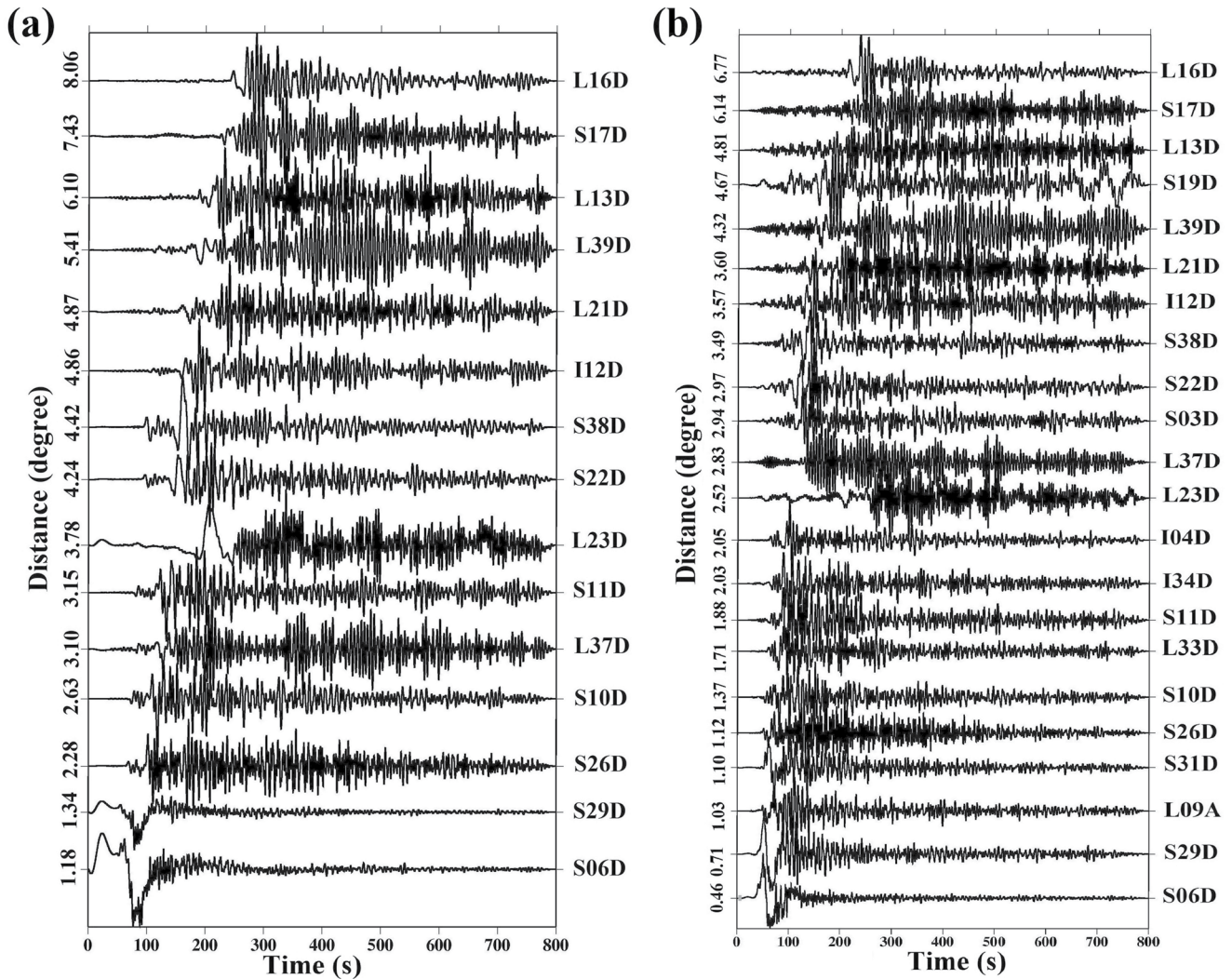
Figure 2. Examples of waveform signals (black) for two selected events from the study region. The corresponding surface wave amplitude values are plotted as a function of distance at different periods (16–40 s) in Figure 3.

spacing of 0.0005. The focal mechanisms are known for the events used in this study, so we use initial values for φ based on the focal mechanism and perform a grid search over ±30° from the initial value in 1° steps.

We invert the 1-D phase velocity and attenuation coefficients for 1-D Vs and Q_μ as a function of depth beneath the region assuming a fixed Vp/Vs ratio and density structure. We use a fixed Vp/Vs of 1.78 and assume an average water depth of 4,000 m for the region. To calculate the predicted phase velocity and attenuation coefficients from a given Q_μ and Vs structure, we use the Computer Programs in Seismology code (Hermann & Ammon, 2004). The code incorporates attenuation effects and can explicitly include a water layer. The program generates the partial derivatives for Vs, and we use a finite difference approximation for the partial derivatives for attenuation coefficients with respect to Vs and Q_μ. We also assume the compressional wave quality factor (Q_P) is approximately double Q_μ, but find this ratio (+/− 50%) has little impact on the result. In the water layer, the code only considers the effect of Q_P on the attenuation coefficient and dispersion. We set Q_P to 900 in the water layer, which remains fixed during the inversion. Testing indicates that smaller values (down to 100) do not significantly alter the results of the inversion, and so we choose a high value as we do not expect water to be a lossy medium. We make no distinction between raypaths that cross the ridge and those that do not as we are only interested in a 1-D regional average for the purposes of this paper. We do not invert for anisotropy or account for its effects and instead assume isotropic velocities. Given the 1-D nature of our result and modeling, we cannot account for the effects of scattering caused by strong lateral velocity variations on the Q_μ observation. Therefore, the apparent Q_μ
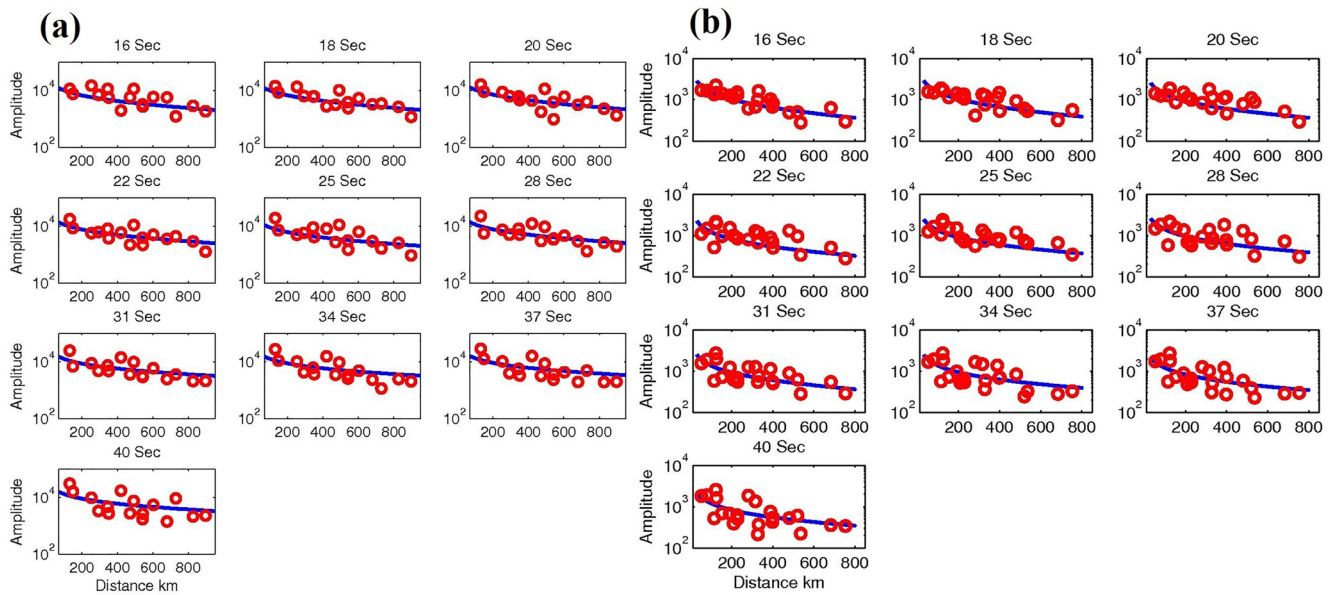
Figure 3. Examples of variations in amplitude with distance. Observed amplitudes (red dots) are plotted as a function of distance for the two example events (panels a and b) shown in Figure 2 at a variety of periods (16–40 s periods at each 2 s period interval). The best fit curve is shown by the blue line.

that we report reflects the effects of both scattering and intrinsic attenuation. We discuss below in greater detail the depths at which our Q_μ model may be more strongly influenced by scattering.

We invert for the reference shear velocity, Vs (ω_0), which is corrected for the effects of attenuation to a frequency of 1 Hz. The reference velocity represents the frequency independent result, as opposed to the apparent Vs at the frequency range of observation if no attenuation is assumed. The code accounts for the effects of physical dispersion via a correction to the phase velocity dispersion that is calculated by integrating over depth the product of attenuation structure and the partial derivatives of phase velocity with respect to the shear and compressional velocity. However, we also present the apparent Vs for comparison to other studies and laboratory predictions that present the apparent Vs. The following relationship can be used to scale the reference Vs to apparent Vs at the frequency range of observation (Kolsky, 1956; Liu et al., 1976):

$$V_s(\omega) = V_s(\omega_0) \left(1 + \frac{1}{\pi Q_\mu} ln \left(\frac{\omega}{\omega_0} \right) \right) \tag{2}$$

where ω is angular frequency and ω_0 is the reference angular frequency. For the frequency range and Q_μ values determined here, the correction between reference Vs and apparent Vs is 1%–2% and encapsulated in the error bars. We note that the apparent Vs is also very similar to the starting Vs model, that is, that reported by Harmon et al. (2020), which did not correct for attenuation (Figure 4).

3. Results

We first plot the seismograms (Figure 2) and the amplitude variations as a function of distance across the array (Figure 3). We also show amplitude variations corrected for geometrical spreading (Figure S1). We find a pattern of decreasing amplitude with increasing distance, which likely results from the combined effects of geometric spreading, source radiation pattern, focusing/scattering, and intrinsic attenuation. Our inversion result and other global and regional results included in our comparisons typically account for geometric spreading and source radiation pattern. There is some scatter in the amplitude which may be related to velocity heterogeneity and associated focusing/scattering and local site effects. We proceed focusing primarily on intrinsic attenuation and considering potential effects from focusing/scattering in cases where the latter provides an explanation for divergent observations.
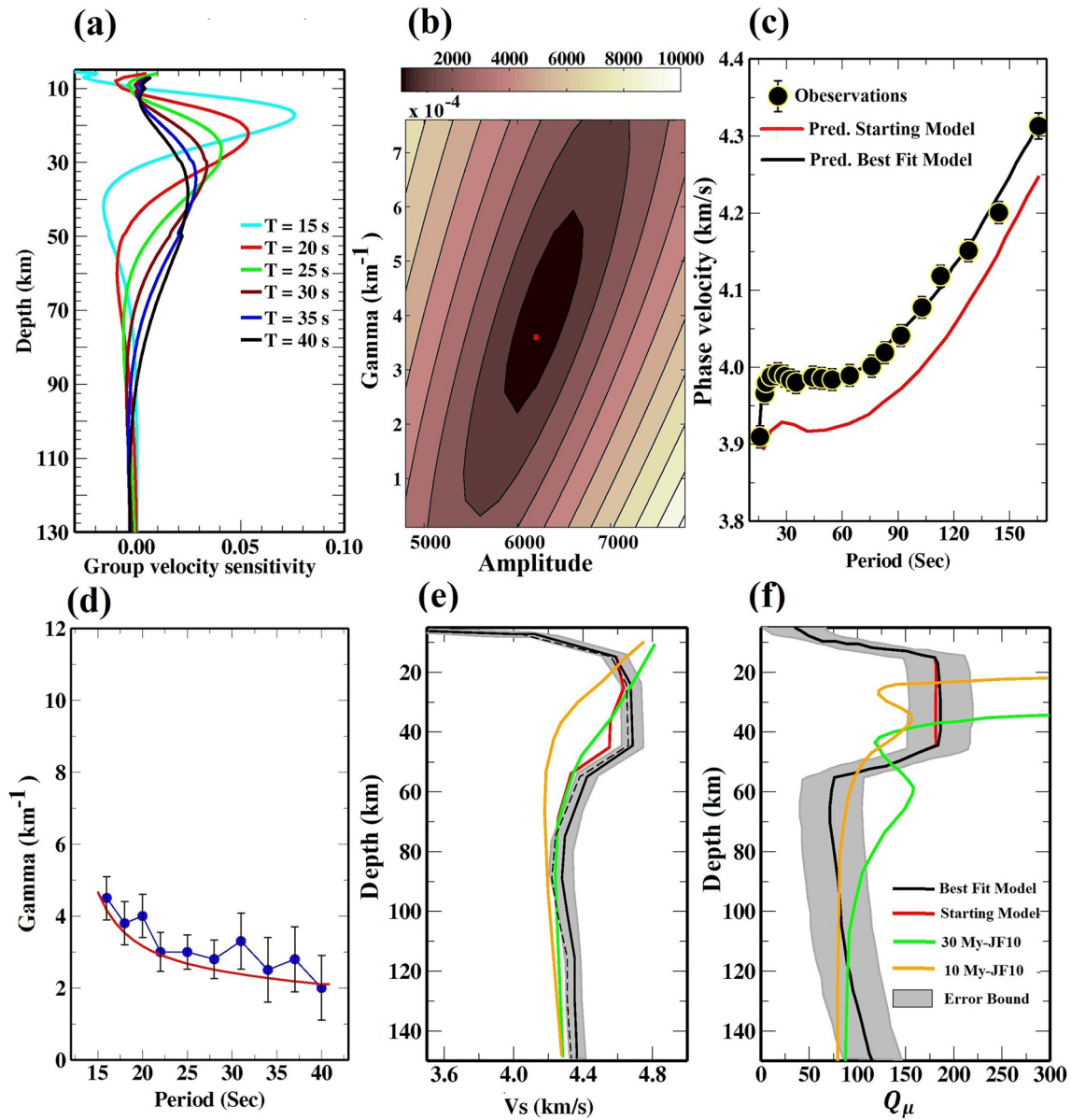
Figure 4. Results summary. (a) Sensitivity kernels of fundamental mode Rayleigh wave group velocities at 15, 20, 25, 30, 35, and 40 s period. (b) One example of a grid search result for attenuation coefficient. (c) Average 1-D phase velocity starting model (red; Harmon et al., 2020; Saikia et al., 2021), observations (black dots), and best fit model (black) (d) Attenuation coefficients determined from Rayleigh waves. Blue line with filled circles shows the observed values and red line is the predicted values from the Qμ model inversion result. (e) Inverted reference Vs (black), error bar of the reference velocity Vs (gray) and apparent Vs (dashed black line) are compared to the starting model (red) and the predicted shear velocity based on the experimental predictions for the half space cooling model from Jackson and Faul (2010) for 30 My (green) and 10 My old lithosphere (orange). (f) Inverted Qμ (black) and error bar (gray) are compared to the predicted Qμ value based on the model of Jackson and Faul (2010) for 30 My (green) and 10 My old lithosphere (orange).

We plot the estimated attenuation coefficients at the period of range from 15–40 s with their associated standard error bars (Figure 4d). The Vs sensitivity curves at different periods are shown in Figure 4a. One example of the grid search result for amplitude and attenuation coefficient for one event at period 18 s is shown in Figure 4b. The grid search result has a clearly defined minimum that provides an error estimate for the individual measurements, and these are propagated through to the error in the average result.

Our observed average attenuation coefficients (γ) vary within the range of 4.5×10^{-4} km^{-1} to 2.0×10^{-4} km^{-1} beneath the study region. Attenuation coefficients decrease with increasing period from 4.5×10^{-4} km^{-1} at 16 s to 3×10^{-4} km^{-1} at 22 s period (Figure 4d). The attenuation varies more smoothly within the range of 2×10^{-4} km^{-1}
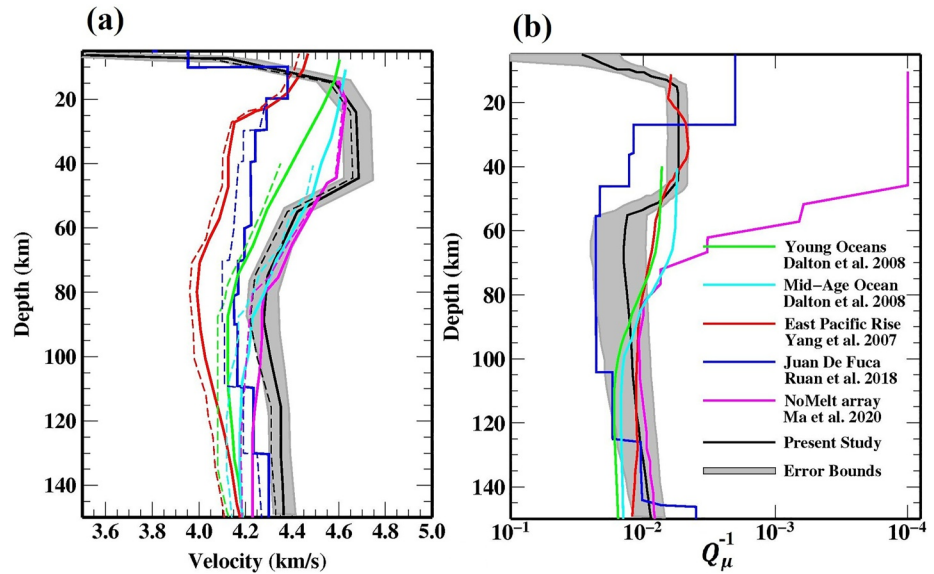
Figure 5. Comparison of average 1-D observations. (a) The best fitting reference Vs (solid lines), reference Vs error (gray) and apparent shear velocity (dashed black) are compared to the other global and regional models (colored lines: solid for reference Vs and dashed for apparent Vs) (b) Q_μ^{-1} (solid black) and Q_μ^{-1} error (gray) from the present study are compared to other global and regional models (colored lines).

and 3×10^{-4} km^{-1} at periods 22–40 s. The standard errors of the attenuation coefficients are significant from zero at all periods. The fits between the observed (black dots) and predicted (red curve) attenuation coefficients are good at all periods (Figure 4d).

The inversion result for Q_μ for the region is shown in Figure 4f along with standard error of the linearized least squares inversion at the final iteration (gray) and the Vs result in Figure 4e again with standard error. In the shallow portion of the crust and upper mantle (4–10 km) Q_μ is low 40 ± 17 and increases to 175 ± 16 at 10 km depth. At lithospheric depths Q_μ varies more smoothly, 175 ± 16 at 10–50 km depth. At greater depths (>60 km), Q_μ varies more uniformly within the range of 75–115. The apparent Vs 1-D profile, that is, the velocity observed for the frequency of interrogation, is similar to that from previous work (Harmon et al., 2020; Saikia et al., 2021). The reference Vs structure, that is, the velocity corrected to the frequency independent version at 1 Hz, is very similar to the apparent Vs structure, but slightly faster, by 1%–2%. The error values of both Vs structures are also the same (0.03–0.07 km/s), but error on the apparent Vs is not shown for clarity.

For comparison, apparent Vs and Q_μ models for 10 and 30 My seafloor predicted for a thermal model by laboratory experiments are shown (Figures 4f and 4g) (Jackson & Faul, 2010). We also compared our results with the EPR (Yang et al., 2007), the Juan de Fuca Ridge (Ruan et al., 2018), old Pacific lithosphere (Ma et al., 2020), PREM (Dziewonski & Anderson, 1981), and a variety of oceanic ages from a global model (Dalton et al., 2008) (Figure 5). We have also examined the Q_μ and apparent Vs relationship of the present study and other studies of oceanic regions in comparison to four different experimental predictions (Jackson & Faul, 2010; McCarthy et al., 2011; Yamauchi & Takei, 2016) using the very broadband rheology calculator (Havlin et al., 2021) (Figure 6). The frequency dependence of shear attenuation in the lithosphere and asthenosphere from previously published results along with the results from the present study is shown in Figure 7

4. Discussion

Our 1-D Q_μ model reflects the general expectations for an oceanic profile. The low Q_μ in the shallowest sub-oceanic layers (4–10 km) is likely dominated by the combined effects of topography and pelagic sediments with low shear moduli and other scattering effects of a heterogeneous crust rather than reflecting intrinsic attenuation. The topography across the region is rough, varying by several km (Harmon et al., 2018), and previous work has suggested that scattering of short period surface waves in the water is strong (Harmon et al., 2009). Therefore, we do not interpret the shallow result any further. The mantle lithosphere (10–50 km) is characterized by high Q_μ
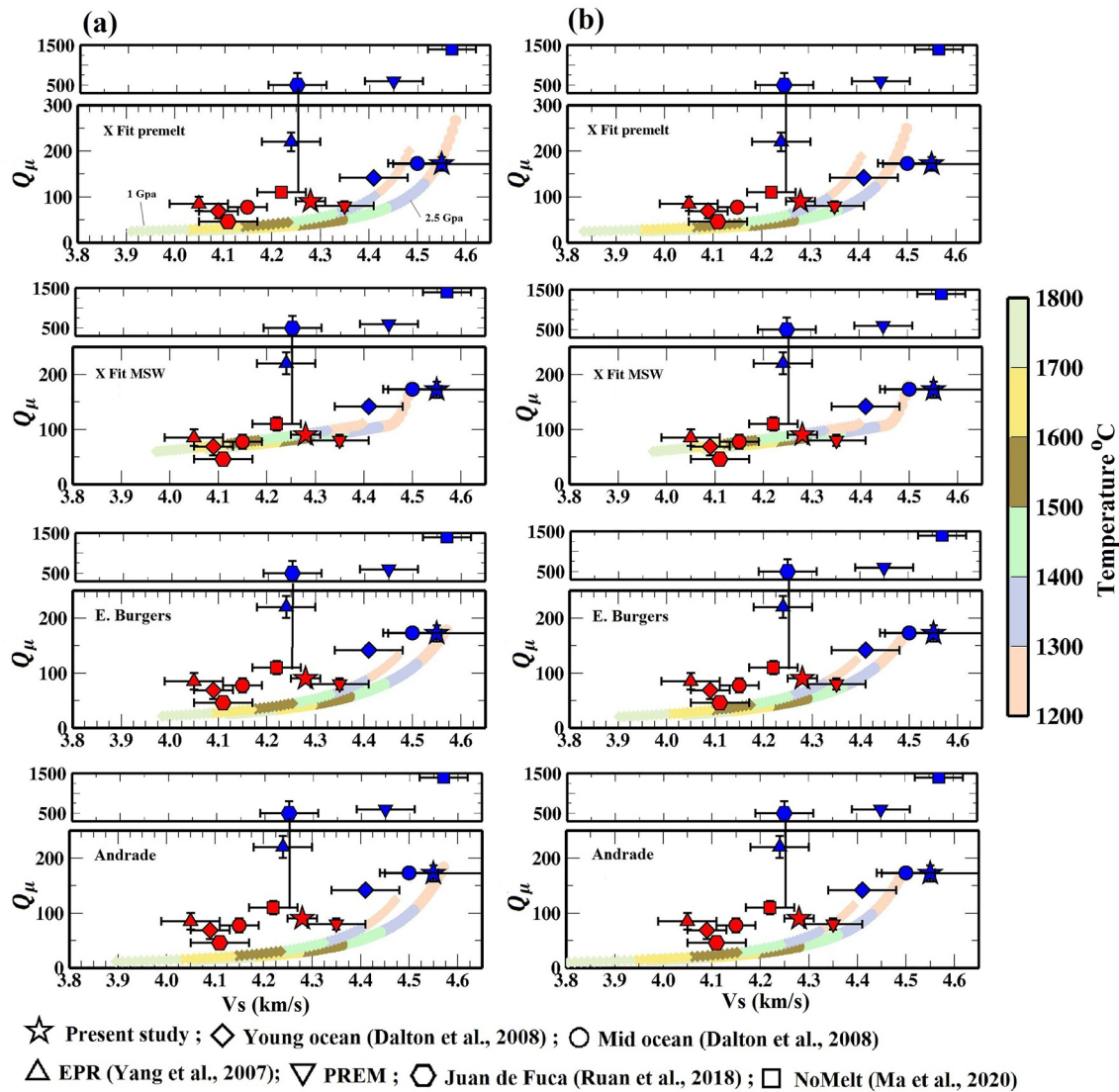
Figure 6. Apparent shear velocity (Vs) and Q_μ from the current study in comparison to observation from other oceanic study regions and four different experimental predictions as a function of temperature. The comparison is shown for predictions for a thermal half space cooling model (a) and also a model that assumes 1% partial melt (b) according to the Takei (1998) wetting angle parameterization for melt and seismic velocity. The experimental predictions are shown for two pressures 1 Gpa (about 32 km depth) and 2.5 Gpa (about 82 km depth) to represent the lithosphere and asthenosphere, respectively. The experimental predictions include the Burgers and Andrade model following Jackson and Faul (2010), X Fit MSW following master-curve Maxwell scaling approaches of McCarthy et al. (2011), and X Fit Premelt following Yamauchi and Takei (2016). Since the PREM model is in terms of reference velocity, here it is adjusted to the average frequency used in this study (15–143 s) for comparison purpose.

(175 ± 16) likely reflecting a cool and rigid plate, at least in comparison to the underlying asthenosphere, which is characterized by lower Q_μ (90 ± 15) owing to higher temperatures and/or other factors which we will discuss further in subsequent paragraphs.

A comparison of our Vs and Q_μ results to the laboratory based predictions provides a reference point for the control of temperature on the structure (Figure 4). Although we present both apparent Vs and reference Vs (Figures 4–6), apparent Vs values are best for comparisons to the laboratory experiments, given that those studies also report apparent Vs (Figures 4 and 6). The Vs predictions for the Jackson and Faul (2010) model are in general slower and outside error of the observed Vs for most depths, although the 30 Myr predictions (orange line, Figure 4e) is within error between 70–100 km depth and 30–40 km depth. The Q_μ predictions for the model are within error for 90–150 km for 30 Myr old seafloor and 50–150 km for 10 Myr old seafloor (Figure 4f). However, the Q_μ model predictions do not consistently match the observations throughout the lithosphere-asthenosphere
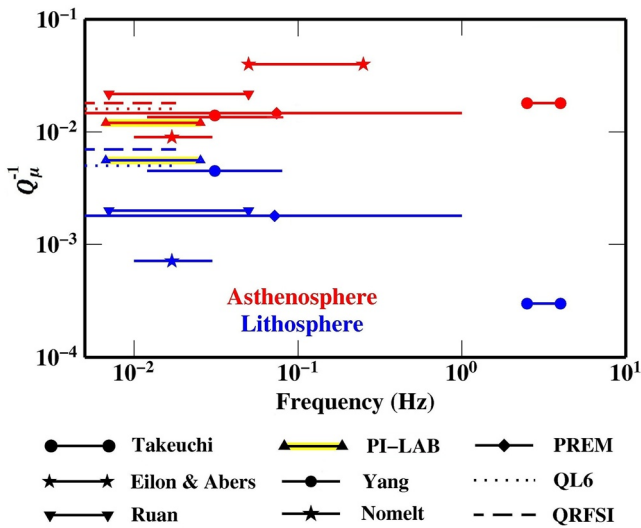
Figure 7. Comparison of the frequency dependence of attenuation in the lithosphere (blue lines) and asthenosphere (red lines) between the present study and the other studies. We compare with the global PREM model and the QL6 model (Durek & Ekström, 1996), the oceanic part of the QRSDI12 model (Dalton et al., 2008), the regional model from the East Pacific Rise region (Yang et al., 2007), regional models from the Juan de Fuca Ridge from body waves (Eilon & Abers, 2017) and surface waves (Ruan et al., 2018), and the regional model beneath the northwestern Pacific region (Takeuchi et al., 2017). The star represents the results of the present study. The result from this study is highlighted in yellow. This figure is modified from Takeuchi et al. (2017).

system (Figure 4f). One of the reasons for the discrepancy could be that the Jackson and Faul (2010) prediction is for the half-space cooling model, which does not account for lateral heat conduction. Geodynamic models that account for lateral heat conduction predict cooler temperatures which would likely be characterized by faster seismic velocities and higher Q_μ beneath slow spreading ridges (Phipps Morgan et al., 1987). In addition, the Jackson and Faul (2010) parameterization is tuned for temperatures >1100°C, so comparisons at $\sim$>50 km are likely the only depths that are valid for comparison (Jackson & Faul, 2010). At depths >50 km our V_s is larger and our Q_μ is lower than predicted by experiments suggesting either that other factors besides temperature may be required or a slightly different parameterization of Vs/Q_μ is needed (Figures 4e and 4f). Other parameterizations of Q_μ^{-1} based on seismic observations of Goes et al. (2012) have been slightly more successful in matching sub-ridge observations in the Pacific. However, again these parameterizations have required additional mechanisms to completely explain the observations. We will explore other parameterizations in a global context below.

The comparison of our Vs result to other in situ studies and global results from oceanic lithosphere highlights the variability of Vs structures (Figure 5a). Near the ridge, spreading rate appears to have a strong effect Vs. The ultrafast spreading EPR at 17°S has the slowest profile overall with the slowest "fast lid" and asthenosphere (Yang et al., 2007). This is followed by the intermediate Juan De Fuca Ridge (Ruan et al., 2018). The global averages are the next fastest profiles, while our profile from the slow spreading Mid-Atlantic Ridge is the fastest overall with some overlap between our result and the mid-age ocean global profile (Dalton et al., 2008). This variation is predicted somewhat based on the relative age and spreading rate, because at slower spreading rates, lateral conductive cooling results in a $\sim$20 km thick lithosphere beneath young seafloor ages (Parmentier & Morgan, 1990). Our result is also similar to that from old Pacific lithosphere originally formed at the fast spreading EPR (Ma et al., 2020).

The comparisons of Q_μ also demonstrate the variability of seismic properties as a function of seafloor age at lithospheric depths, but not necessarily spreading rate, and also not necessarily at asthenospheric depths (Figure 5). At lithospheric depths, even accounting for differences in lithospheric thickness, there is wide variation in Q_μ (150–1,400) from young to very old seafloor. The highest Q_μ (1,400) is associated with the oldest seafloor of NoMelt. The remainder of the lithospheric Q_μ measurements from young seafloor are much smaller, but with no obvious trend in spreading rate. Specifically, our result from the slow spreading Mid-Atlantic Ridge is $Q_\mu = 175 \pm 16$, the result beneath the intermediate spreading Juan de Fuca Ridge is $Q_\mu = 500$ (Ruan et al., 2018), while the result beneath the ultrafast spreading EPR is $Q_\mu = 225$ (Yang et al., 2007). Our result is within error of the ultra-fast spreading EPR. The variability in lithospheric Q_μ beneath ridges, suggests some other process affects the apparent Q_μ of the lithosphere, and it is not necessarily related to spreading rate. For example, lenses of cooled melt and patchy alteration of the lithosphere to greater depths could result in a heterogeneous lithospheric structure, which could cause scattering and a reduced apparent Q_μ in our study area. Asthenospheric Q_μ values for most of the regions are within error of our result at 80–140 km depth (Figure 5).

There are some general trends visible when we compare our results to previously reported Rayleigh wave results for Vs-Q_μ in oceanic regions (Figures 5 and 6). For this comparison, we use the maximum value of Q_μ from smooth inversions in the lithosphere (shown in Figure 5) given that the remainder of studies are also from smooth models. The Q_μ from the smooth parameterisations also likely better reflects the lithospheric mantle since it avoids artifacts from the crust, which may be characterized by high attenuation owing to scattering. However, we expand the error bars in Figure 6 to include the smaller Q_μ values reported from minimum parameterization models (Ruan et al., 2018; Yang et al., 2007). Asthenospheric Q_μ for smooth and minimum parameterization models were within error of each other. Both the Vs and Q_μ values are larger in the lithosphere in comparison to asthenosphere based on all the global observations. In the lithosphere, our result is close to within error

of the global attenuation models from Dalton et al. (2008). Ma et al. (2020) found a high (4.54 ± 0.09 km/s) lithospheric Vs that is similar to our results, with a much greater Q_μ, which could be in the trend of our results and the global models. However, the Yang et al. (2007) result has a slow Vs (4.27 ± 0.05 km/s) relative to Q_μ (225 ± 50), and this is similarly true for Ruan et al. (2018) (Vs = 4.29 ± 0.05 km/s with Q_μ = 500 ± 400). The range of reported Q_μ is larger in the lithosphere (125–1,400) in comparison to the asthenosphere Q_μ (50–100), whereas the range of Vs reported in the lithosphere (4.3–4.6 km/s) is similar to that reported in the asthenosphere (4.1–4.5 km/s), respectively. The asthenospheric results from all studies form a near linear array, given the smaller variability in Q_μ.

We further examine the relationships between the observed Vs and Q_μ and the predictions from 4 different Vs-Q_μ relationships based on laboratory experiments (Figure 6). These include the Andrade and the extended Burghers models of Jackson and Faul (2010), the master curve based on Maxwell relaxation time approach of McCarthy et al. (2011), and the master curve modified for the effects of pre-melt of Yamauchi and Takei (2016). We choose two pressures, 1 GPa (about 32 km depth) and 2.5 GPa (about 82 km depth), to represent the lithosphere and the asthenosphere, respectively. We calculated the predicted Q_μ and Vs for a range of temperatures between 1,200–1,800°C and for a frequency range from 0.01–0.05 Hz, using the Very Broadband Rheology calculator (Havlin et al., 2021) assuming elastic coefficients appropriate for an olivine mantle (Figure 6a). We use the default settings in the calculations, which utilize the same coefficients and assumptions from the original published works. We assume a 1.3 cm grain size in the Andrade, extended Burghers models, which is a free parameter. The grain sizes for the empirical fits from the Maxwell relaxation time master curve and master curve modified for the effects of premelt are fixed at 1 and 4 mm, that is, the values assumed in the original publications in fitting the master curves to seismic observations. The shapes of the master curves (X Fit MSW) are different from the other three predictions with a sharp kink visible near 4.55 km/s. The master curve corrected for pre-melt (X Fit Premelt) has higher Q_μ at< 1,300°C than the other three predictions. We also calculate Q_μ and Vs for the same temperature and pressures, but also allow 1% partial melt (Figure 6b). The effect on Q_μ is minimal, but reduces the velocities by ∼2% based on the Takei (1998) wetting angle parameterization for melt and seismic velocity (Figure 6b).

The observations from the lithosphere generally fall within the range of predictions from laboratory experiments with some exceptions. The Yang et al., (2007) Vs is slower than predicted, and the Ruan et al. (2018), Ma et al. (2020) and PREM (Dziewonski & Anderson, 1981) models have high Q_μ relative to the predictions. The high Q_μ from Ruan et al. (2018) and Ma et al. (2020) might be explained by cooler temperatures than calculated here, but the slow Vs of Ruan et al. (2018) would still remain outside the predictions. The asthenospheric Vs and Q_μ observations fall on top of the laboratory predictions for a thermal model and have a near linear trend, which generally agrees with the laboratory predictions. The Q_μ-Vs observations are in best agreement with the master curve model (X Fit MSW) (Figure 6a). The Q_μ observations for a given Vs are higher than the predictions from the other three parameterisations. However, to explain the observations with temperature variation alone would require a range that would span 1,300–1,800°C. This seems unlikely given that we are considering mid-ocean ridges and "normal" old oceanic lithosphere, that is, not hotspots. The average mantle potential temperature is thought to be 1,310–1,430°C (Sarafian et al., 2015), with only a variation of ±100°C expected in most tectonic environments except for hotspots (Hart et al., 2008; Putirka et al., 2007), although some petrologic/seismic ridge estimates give a range of 1,300–1,550°C (Dalton et al., 2014). In addition, given typical adiabats, mantle temperatures at the depths of these asthenospheric observations do not likely exceed the mantle potential temperature by much (∼< 30–50°C). The addition of 1% melt (Figure 6b), shifts all of the curves to lower velocities, although the mantle temperatures required by some observations are still quite high, up to 1,600–1,700°C. Therefore, partial melt percentages that exceed 1% may be required to explain some of the slow Vs observations while not exceeding expected mantle temperatures. Therefore, adding melt to the system, effectively lowering the Vs relative to the Q_μ, could explain the observations in the asthenosphere. Overall, the master curve model provides the best fit to the observations in the lithosphere and asthenosphere, given the assumptions used here in general, as it does not under predict Q_μ for a given Vs. Other models might be made to fit better by tuning the model parameter choices.

Our lithospheric and asthenospheric Q_μ^{-1} results generally fit into the frequency dependent trends suggested by global comparisons. Our lithospheric Q_μ^{-1} is similar to averages over the ocean basins from longer period global models QL7 and QRFSI12 (Durek & Ekström, 1996; Dalton et al., 2008) (Figure 7). It could be interpreted

as following the trend of decreasing Q_μ^{-1} with increasing frequency suggested for the lithosphere (Takeuchi et al., 2017). In other words our result could broadly be seen as connecting the longer period results (QL7, QRFSI12) to PREM, Juan de Fuca (Ruan et al., 2018) and the higher frequency result of Takeuchi et al. (2017). The NoMelt lithospheric Q_μ^{-1} is smaller and has been interpreted as not necessarily following this trend (Ma et al., 2020). One possibility is that the low Q_μ^{-1} is related to the older and likely cooler lithosphere of NoMelt. Our asthenospheric Q_μ^{-1} broadly falls within the trend of frequency independent Q_μ^{-1} in the asthenosphere. It has been suggested that this is the result of an absorption band peak that falls within the seismic frequency band as a result of a different mechanism (Takeuchi et al., 2017). The effect is likely caused by a different factor in the asthenosphere, such as the presence of partial melt and/or pre-melt conditions. At the same time, our asthenospheric Q_μ^{-1} is slightly smaller than the other results, more similar to NoMelt. One possible explanation is that melt is only present in the asthenosphere over some sections of our study area. This has been suggested based on observations of punctuated anomalies in both shear wave velocities from surface waves (Harmon et al., 2020), magnetotelluric imaging (Wang et al., 2020), seismic imaging guided by magnetotelluric imaging (Harmon, Wang, et al., 2021), and intermittent imaging of sharp discontinuities from receiver functions (Rychert et al., 2021). Overall, the trends from the other studies suggest that no large difference in Q_μ^{-1} in the lithosphere in comparison to the asthenosphere is predicted at the long periods of our study (Figure 7). Therefore, we do not have a strong interpretation of whether our result supports a different frequency dependence of Q_μ^{-1} in the lithosphere in comparison to the asthenosphere. Finer lateral resolution of 3-D Q_μ^{-1} in our study area is required to fully disambiguate if asthenospheric Q_μ^{-1} requires the presence of partial melt in some regions. Similarly, additional attenuation measurements in a variety of locations and at higher frequencies are required to further investigate the attenuation-frequency trends in the lithosphere versus the asthenosphere.

5. Conclusions

We have estimated Q_μ for 0–80 Myr old oceanic lithosphere and asthenosphere beneath and nearby the equatorial Mid-Atlantic Ridge using local Rayleigh waves from 15–40 s period. We find values of 175 ± 16 in the lithosphere and 90 ± 15 in the asthenosphere. Our result agrees with other observations from global models and in situ experiments from a variety of seafloor ages in the Pacific which find higher Q_μ and Vs values in the lithosphere in comparison to the asthenosphere. Q_μ results from previous oceanic studies show a much wider spread in lithospheric Q_μ (125–1,400) than asthenospheric Q_μ (50–100). Comparisons of previous global and regional observations including our result to four different laboratory predictions of Vs and Q_μ for thermal models shows generally good agreement; although, some disparity suggests that a small amount of partial melt is likely required to explain several observations. We find lithospheric Vs estimates are generally faster beneath slower spreading ridges, as expected owing to lateral conductive cooling. However, we find Q_μ beneath ridges is not necessarily dependent on spreading rate and therefore additional factors, such as a component of scattering beneath our study area may be required to reduce Q_μ. Our results could be considered consistent with different frequency dependencies of Q_μ in the lithosphere in comparison to the asthenosphere, although according to the global trends the difference is not expected to be large at the longer periods of our result. Our 1-D average aligns with the predictions from laboratory experiments for a thermal model, and does not require the presence of partial melt, consistent with previous observations that required melt intermittently in our study area. Further investigation of Q_μ regionally and globally in 3-dimensions is required to better constrain this possibility.

Data Availability Statement

All the figures were generated using Generic Mapping Tools v.4.5.0 (www.soest.hawaii.edu/gmt, last accessed December 2014). Data set are available at the IRIS DMC website: https://ds.iris.edu/ds/nodes/dmc/. Data are from network XS 2016 (https://doi.org/10.7914/SN/XS_2016).

References

Abers, G. A., Fischer, K. M., Hirth, G., Wiens, D. A., Plank, T., Holtzman, B. K., et al. (2014). Reconciling mantle attenuation temperature relationships from seismology, petrology, and laboratory measurements. *Geochemistry, Geophysics, Geosystems*, 15, 3521–3542. https://doi.org/10.1002/2014GC005444

Agius, M. R., Harmon, N., Rychert, C. A., Tharimena, S., & Kendall, J. M. (2018). Sediment characterization at the equatorial mid-atlantic ridge from P-to-S teleseismic phase conversions recorded on the PI-LAB experiment. *Geophysical Research Letters*, 45, 12234–12252. https://doi.org/10.1029/2018GL080565

Agius, M. R., Rychert, C. A., Harmon, N., Tharimena, S., & Kendall, J. M. (2021). A thin mantle transition zone beneath the equatorial Mid-Atlantic Ridge. *Nature*, 589, 562–566. https://doi.org/10.1038/s41586-020-03139-x

Akuhara, T., Nakahigashi, K., Shinohara, M., Yamada, T., Shiobara, H., Yamashita, Y., et al. (2021). Lithosphere-asthenosphere boundary beneath the Sea of Japan from transdimensional inversion of S-receiver functions. *Earth Planets and Space*, 73. https://doi.org/10.1186/s40623-021-01501-5

Albarède, F. (1998). Time-dependent models of U-Th-He and K-Ar evolution and the layering of mantle convection. *Chemical Geology*, 145, 413–429. https://doi.org/10.1016/S0009-2541(97)00152-6

Artemieva, I. M. (2006). Global 1° × 1° thermal model TC1 for the continental lithosphere: Implications for lithosphere secular evolution. *Tectonophysics*, 416, 245–277. https://doi.org/10.1016/j.tecto.2005.11.022

Auer, L., Boschi, L., Becker, T. W., Nissen-Meyer, T., & Giardini, D. (2014). Savani: A variable resolution whole-mantle model of anisotropic shear velocity variations based on multiple data sets. *Journal of Geophysical Research: Solid Earth*, 119, 3006–3034. https://doi.org/10.1002/2013JB010773

Begbein, C., Yuan, K., Schmerr, N., & Xing, Z. (2014). Changes in seismic anisotropy shed light on the nature of the Gutenberg discontinuity. *Science*, 343, 1237–1240. https://doi.org/10.1126/science.1246724

Bogiatzis, P., Karamitrou, A., Neale, J. W., Harmon, N., Rychert, C. A., & Srokosz, M. (2020). Source regions of infragravity waves recorded at the bottom of the Equatorial Atlantic Ocean, using OBS of the PI-LAB Experiment. *Journal of Geophysical Research: Oceans*, 125. https://doi.org/10.1029/2019JC015430

Burgos, J. M., Buhl-Mortensen, L., Buhl-Mortensen, P., Ólafsdóttir, S. H., Steingrund, P., Ragnarsson, S., & Skagseth, Ø. (2020). Predicting the distribution of indicator taxa of vulnerable Marine ecosystems in the Arctic and Sub-arctic Waters of the Nordic Seas. *Frontiers in Marine Science*, 7. https://doi.org/10.3389/fmars.2020.00131

Clark, A. N., & Lesher, C. E. (2017). Elastic properties of silicate melts: Implications for low velocity zones at the Lithosphere-Asthenosphere Boundary. *Science Advances*, 3. https://doi.org/10.1126/sciadv.1701312

Cline, C. J., Faul, U. H., David, E. C., Berry, A. J., & Jackson, I. (2018). Redox-influenced seismic properties of uppermantle olivine. *Nature*, 555, 355–358. https://doi.org/10.1038/nature25764

Dalton, C. A., Ekström, G., & Dziewoński, A. M. (2008). The global attenuation structure of the upper mantle. *Journal of Geophysical Research: Solid Earth*, 113, B09303. https://doi.org/10.1029/2007JB005429

Dalton, C. A., Langmuir, C. H., & Gale, A. (2014). Geophysical and geochemical evidence for deep temperature variations beneath mid-ocean ridges. *Science*, 344, 80–83. https://doi.org/10.1126/science.1249466

Durek, J. J., & Ekström, G. (1996). A radial model of anelasticity consistent with long-period surface-wave attenuation. *Bulletin of the Seismological Society of America*, 86, 144–158.

Dziewonski, A. M., & Anderson, D. L. (1981). Preliminary reference Earth model. *Physics of the Earth and Planetary Interiors*, 25, 297–356. https://doi.org/10.1016/0031-9201(81)90046-7

Eaton, D. W., Darbyshire, F., Evans, R. L., Grütter, H., Jones, A. G., & Yuan, X. (2009). The elusive lithosphere-asthenosphere boundary (LAB) beneath cratons. *Lithos*, 109, 1–22. https://doi.org/10.1016/j.lithos.2008.05.009

Eberhart-Phillips, D., Bannister, S., & Reyners, M. (2020). Attenuation in the mantle wedge beneath super-volcanoes of the taupo volcanic zone, New Zealand. *Geophysical Journal International*, 220, 703–723. https://doi.org/10.1093/gji/ggz455

Eberhart-Phillips, D., Reyners, M., Faccenda, M., & Naliboff, J. (2013). Along-strike variation in subducting plate seismicity and mantle wedge attenuation related to fluid release beneath the North Island, New Zealand. *Physics of the Earth and Planetary Interiors*, 225, 12–27. https://doi.org/10.1016/j.pepi.2013.10.002

Eilon, Z. C., & Abers, G. A. (2017). High seismic attenuation at a mid-ocean ridge reveals the distribution of deep melt. *Science Advances*, 3. https://doi.org/10.1126/sciadv.1602829

Evans, R. L., Hirth, G., Baba, K., Forsyth, D., Chave, A., & Mackie, R. (2005). Geophysical evidence from the MELT area for compositional controls on oceanic plates. *Nature*, 437, 249–252. https://doi.org/10.1038/nature04014

Faul, U. H., Fitz Gerald, J. D., & Jackson, I. (2004). Shear wave attenuation and dispersion in melt-bearing olivine polycrystals: 2. Microstructural interpretation and seismological implications. *Journal of Geophysical Research: Solid Earth*, 109, B06202. https://doi.org/10.1029/2003JB002407

Faul, U. H., & Jackson, I. (2005). The seismological signature of temperature and grain size variations in the upper mantle. *Earth and Planetary Science Letters*, 234(1–2), 119–134. https://doi.org/10.1016/j.epsl.2005.02.008

Fischer, K., Rychert, C. A., Dalton, C., Miller, M., Begbein, C., & Schutt, D. (2020). A comparison of oceanic and continental mantle lithosphere. *Physics of the Earth and Planetary Interiors*, 309, 106600. https://doi.org/10.1016/j.pepi.2020.106600

Fischer, K. M., Ford, H. A., Abt, D. L., & Rychert, C. A. (2010). The lithosphere-asthenosphere boundary. *Annual Review of Earth and Planetary Sciences*, 38, 551–575. https://doi.org/10.1146/annurev-earth-040809-152438

Ford, H. A., Fischer, K. M., Abt, D. L., Rychert, C. A., & Elkins-Tanton, L. T. (2010). The lithosphere-asthenosphere boundary and cratonic lithospheric layering beneath Australia from Sp wave imaging. *Earth and Planetary Science Letters*, 300, 299–310. https://doi.org/10.1016/j.epsl.2010.10.007

Forsyth, D. W. (1992). *Geophysical constraints on mantle flow and melt generation beneath mid-ocean ridges* (pp. 1–65). https://doi.org/10.1029/gm071p0001

Forsyth, D. W., Scheirer, D. S., Webb, S. C., Dorman, L. M., Orcutt, J. A., Harding, A. J., et al. (1998). Imaging the deep seismic structure beneath a mid-ocean ridge: The MELT experiment: The MELT seismic team. *Science*, 280, 1215–1218. https://doi.org/10.1126/science.280.5367.1215

Gaherty, J. B., Jordan, T. H., & Gee, L. S. (1996). Seismic structure of the upper mantle in a central Pacific corridor. *Journal of Geophysical Research: Solid Earth*, 101, 22291–22309. https://doi.org/10.1029/96jb01882

Gale, A., Dalton, C. A., Langmuir, C. H., Su, Y., & Schilling, J. G. (2013). The mean composition of ocean ridge basalts. *Geochemistry, Geophysics, Geosystems*, 14, 489–518. https://doi.org/10.1029/2012GC004334

Goes, S., Armitage, J., Harmon, N., Smith, H., & Huismans, R. (2012). Low seismic velocities below mid-ocean ridges: Attenuation versus melt retention. *Journal of Geophysical Research B: Solid Earth*, *117*, B12403. https://doi.org/10.1029/2012JB009637

Hammond, W. C., & Humphreys, E. D. (2000). Upper mantle seismic wave velocity: Effects of realistic partial melt geometries. *Journal of Geophysical Research*, *105*, 10975–10986. https://doi.org/10.1029/2000jb900041

Hannemann, K., Kruger, F., Dahm, T., & Lange, D. (2017). Structure of the oceanic lithosphere and upper mantle north of the Gloria Fault in the eastern mid-Atlantic by receiver function analysis. *Journal of Geophysical Research*, *122*, 7927–7950. https://doi.org/10.1002/2016jb013582

Harmon, N., Forsyth, D. W., & Weeraratne, D. S. (2009). Thickening of young Pacific lithosphere from high-resolution Rayleigh wave tomography: A test of the conductive cooling model. *Earth and Planetary Science Letters*, *278*, 96–106. https://doi.org/10.1016/j.epsl.2008.11.025

Harmon, N., Rychert, C., Agius, M., Tharimena, S., Le Bas, T., Kendall, J. M., & Constable, S. (2018). Marine Geophysical Investigation of the Chain Fracture Zone in the Equatorial Atlantic From the PI-LAB Experiment. *Journal of Geophysical Research: Solid Earth*, *123*, 11016–11030. https://doi.org/10.1029/2018JB015982

Harmon, N., Rychert, C. A., Constable, S., & Kendall, J. M. (2021). One-sided joint inversion of shear velocity and resistivity from the PI-LAB experiment at the Mid Atlantic Ridge. *Earth and Space Sceince Open Archive*. https://doi.org/10.1002/essoar.10506813.1

Harmon, N., Rychert, C. A., Kendall, J. M., Agius, M., Bogiatzis, P., & Tharimena, S. (2020). Evolution of the oceanic lithosphere in the Equatorial Atlantic from rayleigh wave tomography, evidence for small-scale convection from the PI-LAB experiment. *Geochemistry, Geophysics, Geosystems*, *21*, e2020GC009174. https://doi.org/10.1029/2020GC009174

Harmon, N., Wang, S., Rychert, C. A., Constable, S., & Kendall, J. M. (2021). Shear velocity inversion guided by resistivity structure from the PI-LAB experiment for integrated estimates of partial melt in the mantle. *Journal of Geophysical Research*, *126*, e2021JB022202. https://doi.org/10.1029/2021JB022202

Hart, S. R., Kurz, M. D., & Wang, Z. (2008). Scale length of mantle heterogeneities: Constraints from helium diffusion. *Earth and Planetary Science Letters*, *269*, 508–517. https://doi.org/10.1016/j.epsl.2008.03.010

Havlin, C., Holtzman, B. K., & Hopper, E. (2021). Inference of thermodynamic state in the asthenosphere from anelastic properties, with applications to North American upper mantle. *Physics of the Earth and Planetary Interiors*, *314*, 106639. https://doi.org/10.1016/j.pepi.2020.106639

Hermann, R. B., & Ammon, C. J. (2004). *Surface wave, receiver function and crustal structure. Computer programs in Seismology*. Version 3.30. St. Louis University

Hicks, S. P., Okuwaki, R., Steinberg, A., Rychert, C. A., Harmon, N., Abercrombie, R., et al. (2020). Back-propagating super-shear rupture in the 2016 M7.1 Romanche transform fault earthquake. *Nature Geoscience*, *13*, 647–653. https://doi.org/10.1038/s41561-020-0619-9

Holtzman, B. K., Kohlstedt, D. L., Zimmerman, M. E., Heidelbach, F., Hiraga, T., & Hustoft, J. (2003). Melt segregation and strain partitioning: Implications for seismic anisotropy and mantle flow. *Science*, *301*, 1227–1230. https://doi.org/10.1126/science.1087132

Jackson, I., & Faul, U. H. (2010). Grainsize-sensitive viscoelastic relaxation in olivine: Towards a robust laboratory-based model for seismological application. *Physics of the Earth and Planetary Interiors*, *183*, 151–163. https://doi.org/10.1016/j.pepi.2010.09.005

Johansen, S. E., Panzner, M., Mittet, R., Amundsen, H. E. F., Lim, A., Vik, E., et al. (2019). Deep electrical imaging of the ultraslow-spreading Mohns Ridge. *Nature*, *567*, 379–383. https://doi.org/10.1038/s41586-019-1010-0

Karato, S. I., & Park, J. (2019). *On the origin of the upper mantle seismic discontinuities*. Lithospheric Discontinuities, (pp. 5–34). https://doi.org/10.1002/9781119249740.ch1

Kawakatsu, H., Kumar, P., Takei, Y., Shinohara, M., Kanazawa, T., Araki, E., & Suyehiro, K. (2009). Seismic evidence for sharp lithosphere-asthenosphere boundaries of oceanic plates. *Science*, *324*, 499–502. https://doi.org/10.1126/science.1169499

Key, K., Constable, S., Liu, L., & Pommier, A. (2013). Electrical image of passive mantle upwelling beneath the northern East Pacific Rise. *Nature*, *495*, 499–502. https://doi.org/10.1038/nature11932

Klein, E. M., & Langmuir, C. H. (1987). Global correlations of ocean ridge basalt chemistry with axial depth and crustal thickness. *Journal of Geophysical Research*, *92*, 8089. https://doi.org/10.1029/JB092iB08p08089

Ko, Y. T., Kuo, B. Y., Wang, K. L., Lin, S. C., & Hung, S. H. (2012). The Southwestern edge of the Ryukyu subduction zone: A high Q mantle wedge. *Earth and Planetary Science Letters*, *335–336*, 145–153. https://doi.org/10.1016/j.epsl.2012.04.041

Kolsky, H. (1956). LXXI. The propagation of stress pulses in viscoelastic solids. *The Philosophical Magazine. A Journal of Theoretical Experimental and Applied Physic*, *1*, 693–710. https://doi.org/10.1080/14786435608238144

Kumar, P., & Kawakatsu, H. (2011). Imaging the seismic lithosphere-asthenosphere boundary of the oceanic plate. *Geochemistry, Geophysics, Geosystems*, *12*, Q01006. https://doi.org/10.1029/2010GC003358

Leptokaropoulos, K., Harmon, N., Hicks, S., Rychert, C. A., Schlaphorst, D., & Kendall, J. M. (2021). Tidal triggering of microseismicity at the Equatorial Mid-Atlantic Ridge, Inferred from the PI-LAB experiment. *Journal of Geophysical Research*, *126*, e2021JB022251. https://doi.org/10.1029/2021JB022251

Liu, H. P., Anderson, D. L., & Kanamori, H. (1976). Velocity dispersion due to anelasticity: Implications for seismology and mantle composition. *Geophysical Journal International*, *47*, 41–58. https://doi.org/10.1111/j.1365-246X.1976.tb01261.x

Ma, Z., Dalton, C. A., Russell, J. B., Gaherty, J. B., Hirth, G., & Forsyth, D. W. (2020). Shear attenuation and anelastic mechanisms in the central Pacific upper mantle. *Earth and Planetary Science Letters*, *536*, 116148. https://doi.org/10.1016/j.epsl.2020.116148

Mark, H. F., Collins, J. A., Lizarralde, D., Hirth, G., Gaherty, J. B., Evans, R. L., & Behn, M. D. (2021). Constraints on the depth, thickness, and strength of the G discontinuity in the Central Pacific from S receiver functions. *Journal of Geophysical Research*, *126*, e2019JB019256. https://doi.org/10.1029/2019JB019256

McCarthy, C., Takei, Y., & Hiraga, T. (2011). Experimental study of attenuation and dispersion over a broad frequency range: 2. The universal scaling of polycrystalline materials. *Journal of Geophysical Research: Solid Earth*, *116*, B09207. https://doi.org/10.1029/2011JB008384

Mckenzie, D., & Bickle, M. J. (1988). The volume and composition of melt generated by extension of the lithosphere. *Journal of Petrology*, *29*, 625–679. https://doi.org/10.1093/petrology/29.3.625

Mitchell, B. J. (1995). Anelastic structure and evolution of the continental crust and upper mantle from seismic surface wave attenuation. *Reviews of Geophysics*, *33*, 441–462. https://doi.org/10.1029/95RG02074

Mehouachi, F., & Singh, S. C. (2018). Water-rich sublithospheric melt channel in the equatorial Atlantic Ocean. *Nature Geoscience*, *11*. https://doi.org/10.1038/s41561-017-0034-z

Myers, S. C., Beck, S., Zandt, G., & Wallace, T. (1998). Lithospheric-scale structure across the Bolivian Andes from tomographic images of velocity and attenuation for P and S waves. *Journal of Geophysical Research: Solid Earth*, *103*, 21233–21252. https://doi.org/10.1029/98jb00956

Naif, S., Key, K., Constable, S., & Evans, R. L. (2013). Melt-rich channel observed at the lithosphere-asthenosphere boundary. *Nature*, *495*. https://doi.org/10.1038/nature11939

Nettles, M., & Dziewoński, A. M. (2008). Radially anisotropic shear velocity structure of the upper mantle globally and beneath North America. *Journal of Geophysical Research: Solid Earth*, *113*, B02303. https://doi.org/10.1029/2006JB004819

Ni, H., Keppler, H., & Behrens, H. (2011). Electrical conductivity of hydrous basaltic melts: Implications for partial melting in the upper mantle. *Contributions to Mineralogy and Petrology*, *162*, 637–650. https://doi.org/10.1007/s00410-011-0617-4

Nishimura, C. E., & Forsyth, D. W. (1988). Rayleigh wave phase velocities in the Pacific with implications for azimuthal anisotropy and lateral heterogeneities. *Geophysical Journal*, *94*, 479–501. https://doi.org/10.1111/j.1365-246X.1988.tb02270.x

Nishimura, C. E., & Forsyth, D. W. (1989). The anisotropic structure of the upper mantle in the Pacific. *Geophysical Journal International*, *96*, 203–229. https://doi.org/10.1111/j.1365-246X.1989.tb04446.x

Parmentier, E. M., & Morgan, J. P. (1990). Spreading rate dependence of three-dimensional structure in oceanic spreading centres. *Nature*, *348*, 325–328. https://doi.org/10.1038/348325a0

Parsons, B., & Sclater, J. G. (1977). An analysis of the variation of ocean floor bathymetry and heat flow with age. *Journal of Geophysical Research*, *82*, 803–827. https://doi.org/10.1029/jb082i005p00803

Phipps Morgan, J., Parmentier, E. M., & Lin, J. (1987). Mechanisms for the origin of mid-ocean ridge axial topography: Implications for the thermal and mechanical structure of accreting plate boundaries. *Journal of Geophysical Research*, *92*, 12823–12836. https://doi.org/10.1029/jb092ib12p12823

Pozgay, S. H., Wiens, D. A., Conder, J. A., Shiobara, H., & Sugioka, H. (2009). Seismic attenuation tomography of the Mariana subduction system: Implications for thermal structure, volatile distribution, and slow spreading dynamics. *Geochemistry, Geophysics, Geosystems*, *10*, Q04X05. https://doi.org/10.1029/2008GC002313

Priestley, K., & McKenzie, D. (2013). The relationship between shear wave velocity, temperature, attenuation and viscosity in the shallow part of the mantle. *Earth and Planetary Science Letters*, *381*, 78–91. https://doi.org/10.1016/j.epsl.2013.08.022

Putirka, K. D., Perfit, M., Ryerson, F. J., & Jackson, M. G. (2007). Ambient and excess mantle temperatures, olivine thermometry, and active vs. passive upwelling. *Chemical Geology*, *241*, 177–206. https://doi.org/10.1016/j.chemgeo.2007.01.014

Qin, Y., Singh, S. C., Grevemeyer, I., Marjanović, M., & Roger Buck, W. (2020). Discovery of flat seismic reflections in the mantle beneath the young Juan de Fuca Plate. *Nature Communications*, *11*. https://doi.org/10.1038/s41467-020-17946-3

Reeves, Z., Lekić, V., Schmerr, N., Kohler, M., & Weeraratne, D. (2015). Lithospheric structure across the California Continental Borderland from receiver functions. *Geochemistry, Geophysics, Geosystems*, *16*, 246–266. https://doi.org/10.1002/2014GC005617

Ritzwoller, M. H., Shapiro, N. M., & Zhong, S. J. (2004). Cooling history of the Pacific lithosphere. *Earth and Planetary Science Letters*, *226*, 69–84. https://doi.org/10.1016/j.epsl.2004.07.032

Ruan, Y., Forsyth, D. W., & Bell, S. W. (2018). Shear attenuation beneath the Juan de Fuca plate: Implications for mantle flow and dehydration. *Earth and Planetary Science Letters*, *496*, 189–197. https://doi.org/10.1016/j.epsl.2018.05.035

Rychert, C. A., Fischer, K. M., Abers, G. A., Plank, T., Syracuse, E., Protti, J. M., et al. (2008). Strong along-arc variations in attenuation in the mantle wedge beneath Costa Rica and Nicaragua. *Geochemistry, Geophysics, Geosystems*, *9*, Q10S10. https://doi.org/10.1029/2008GC002040

Rychert, C. A., Fischer, K. M., & Rondenay, S. (2005). A sharp lithosphere-asthenosphere boundary imaged beneath eastern North America. *Nature*, *436*, 542–545. https://doi.org/10.1038/nature03904

Rychert, C. A., Harmon, N., Constable, S., & Wang, S. (2020). The Nature of the Lithosphere-Asthenosphere Boundary. *Journal of Geophysical Research: Solid Earth*, *125*, e2018JB016463. https://doi.org/10.1029/2018JB016463

Rychert, C. A., Harmon, N., & Tharimena, S. (2018a). Scattered wave imaging of the oceanic plate in cascadia. *Science Advances*, *4*. https://doi.org/10.1126/sciadv.aao1908

Rychert, C. A., Harmon, N., & Tharimena, S. (2018b). Seismic imaging of the base of the ocean plates. In H. Yuan (Ed.), *Lithospheric discontinuities* (pp. 71–87). AGU Monographs. https://doi.org/10.1002/9781119249740.ch4

Rychert, C. A., Kendall, J. M., & Harmon, N. (2016). *Passive imaging of the lithosphere- asthenosphere boundary*. https://doi.org/10.7914/SN/XS_2016

Rychert, C. A., Rondenay, S., & Fischer, K. M. (2007). P-to-S and S-to-P imaging of a sharp lithosphere-asthenosphere boundary beneath eastern North America. *Journal of Geophysical Research*, *112*, B08314. https://doi.org/10.1029/2006JB004619

Rychert, C. A., & Shearer, P. M. (2009). A global view of the lithosphere-asthenosphere boundary. *Science*, *324*. https://doi.org/10.1126/science.1169754

Rychert, C. A., & Shearer, P. M. (2011). Imaging the lithosphere-asthenosphere boundary beneath the Pacific using SS waveform modeling. *Journal of Geophysical Research: Solid Earth*, *116*, B07307. https://doi.org/10.1029/2010JB008070

Rychert, C. A., Shearer, P. M., & Fischer, K. M. (2010). Scattered wave imaging of the lithosphere-asthenosphere boundary. *Lithos*, *120*, 173–185. https://doi.org/10.1016/j.lithos.2009.12.006

Rychert, C. A., Tharimena, S., Harmon, N., Wang, S., Constable, S., Kendall, J. M., et al. (2021). A dynamic lithosphere–asthenosphere boundary near the equatorial Mid-Atlantic Ridge. *Earth and Planetary Science Letters*, *566*, 116949. https://doi.org/10.1016/j.epsl.2021.116949

Saikia, U., Rychert, C., Harmon, N., & Kendall, J. M. (2020). Sediment structure at the equatorial mid-atlantic ridge constrained by seafloor admittance using data from the PI-LAB experiment. *Marine Geophysical Researches*, *41*. https://doi.org/10.1007/s11001-020-09402-0

Saikia, U., Rychert, C., Harmon, N., & Kendall, J. M. (2021). Upper mantle anisotropic shear velocity structure at the equatorial Mid-Atlantic ridge constrained by rayleigh wave group velocity analysis from the PI-LAB experiment. *Geochemistry, Geophysics, Geosystems*, *22*, e2020GC009495. https://doi.org/10.1029/2020GC009495

Sarafian, E., Evans, R. L., Collins, J. A., Elsenbeck, J., Gaetani, G. A., Gaherty, J. B., et al. (2015). The electrical structure of the central Pacific upper mantle constrained by the NoMelt experiment. *Geochemistry, Geophysics, Geosystems*, *16*, 1115–1132. https://doi.org/10.1002/2014GC005709

Schmerr, N. (2012). The Gutenberg discontinuity: Melt at the lithosphere-asthenosphere boundary. *Science*, *335*, 1480–1483. https://doi.org/10.1126/science.1215433

Schurr, B., Asch, G., Rietbrock, A., Trumbull, R., & Haberland, C. (2003). Complex patterns of fluid and melt transport in the central Andean subduction zone revealed by attenuation tomography. *Earth and Planetary Science Letters*, *215*, 105–119. https://doi.org/10.1016/S0012-821X(03)00441-2

Shapiro, N. M., & Ritzwoller, M. H. (2002). Monte-Carlo inversion for a global shear-velocity model of the crust and upper mantle. *Geophysical Journal International*, *151*, 88–105. https://doi.org/10.1046/j.1365-246X.2002.01742.x

Stachnik, J. C., Abers, G. A., & Christensen, D. H. (2004). Seismic attenuation and mantle wedge temperatures in the Alaska subduction zone. *Journal of Geophysical Research: Solid Earth*, *109*, B10304. https://doi.org/10.1029/2004JB003018

Stein, C. A., & Stein, S. (1992). A model for the global variation in oceanic depth and heat flow with lithospheric age. *Nature*, *359*. https://doi.org/10.1038/359123a0

Stern, T. A., Henrys, S. A., Okaya, D., Louie, J. N., Savage, M. K., Lamb, S., et al. (2015). A seismic reflection image for the base of a tectonic plate. *Nature*, *518*. https://doi.org/10.1038/nature14146

Syracuse, E. M., Abers, G. A., Fischer, K., MacKenzie, L., Rychert, C., Protti, M., et al. (2008). Seismic tomography and earthquake locations in the Nicaraguan and Costa Rican upper mantle. *Geochemistry, Geophysics, Geosystems*, *9*, Q07S08. https://doi.org/10.1029/2008GC001963

Takanami, T., Selwyn Sacks, I., & Hasegawa, A. (2000). Attenuation structure beneath the volcanic front in northeastern Japan from broad-band seismograms. *Physics of the Earth and Planetary Interiors*. https://doi.org/10.1016/S0031-9201(00)00169-2

Takei, Y. (1998). Constitutive mechanical relations of solid-liquid composites in terms of grain-boundary contiguity. *Journal of Geophysical Research: Solid Earth*, *103*, 18183–18203. https://doi.org/10.1029/98jb01489

Takeuchi, N., Kawakatsu, H., Shiobara, H., Isse, T., Sugioka, H., Ito, A., & Utada, H. (2017). Determination of intrinsic attenuation in the oceanic lithosphere-asthenosphere system. *Science*, *358*. https://doi.org/10.1126/science.aao3508

Tan, Y., & Helmberger, D. V. (2007). Trans-Pacific upper mantle shear velocity structure. *Journal of Geophysical Research: Solid Earth*, *103*, 18183–18203. https://doi.org/10.1029/2006JB004853

Tharimena, S., Rychert, C., & Harmon, N. (2017). A unified continental thickness from seismology and diamonds suggests a melt-defined plate. *Science*, *357*. https://doi.org/10.1126/science.aan0741

Tonegawa, T., Miura, S., Ishikawa, A., Sano, T., Suetsugu, D., Isse, T., et al. (2019). Characterization of crustal and uppermost-mantle seismic discontinuities in the Ontong Java Plateau. *Journal of Geophysical Research*, *124*, 7155–7170. https://doi.org/10.1029/2018jb016970

Tsumura, N., Matsumoto, S., Horiuchi, S., & Hasegawa, A. (2000). Three-dimensional attenuation structure beneath the northeastern Japan arc estimated from spectra of small earthquakes. *Tectonophysics*, *319*. https://doi.org/10.1016/S0040-1951(99)00297-8

Turner, S., & Hawkesworth, C. (1997). Constraints on flux rates and mantle dynamics beneath island arcs from Tonga-Kermadec lava geochemistry. *Nature*, *389*. https://doi.org/10.1038/39257

Wang, S., Constable, S., Rychert, C. A., & Harmon, N. (2020). A lithosphere-asthenosphere boundary and partial melt estimated using marine magnetotelluric data at the Central Middle Atlantic Ridge. *Geochemistry, Geophysics, Geosystems*, *21*, e2020GC009177. https://doi.org/10.1029/2020gc009177

Wei, S. S., & Wiens, D. A. (2018). P-wave attenuation structure of the Lau back-arc basin and implications for mantle wedge processes. *Earth and Planetary Science Letters*, *502*. https://doi.org/10.1016/j.epsl.2018.09.005

Wei, S. S., Wiens, D. A., Zha, Y., Plank, T., Webb, S. C., Blackman, D. K., et al. (2015). Seismic evidence of effects of water on melt transport in the Lau back-arc mantle. *Nature*, *518*. https://doi.org/10.1038/nature14113

Yamauchi, H., & Takei, Y. (2016). Polycrystal anelasticity at near-solidus temperatures. *Journal of Geophysical Research: Solid Earth*, *121*, 7790–7820. https://doi.org/10.1002/2016JB013316

Yang, Y., Forsyth, D. W., & Weeraratne, D. S. (2007). Seismic attenuation near the East Pacific Rise and the origin of the low-velocity zone. *Earth and Planetary Science Letters*, *258*. https://doi.org/10.1016/j.epsl.2007.03.040

Zhang, Z. Q., & Olugboji, T. (2021). The signature and elimination of sediment reverberations on submarine receiver functions. *Journal of Geophysical Research*, *126*, e2020JB021567. https://doi.org/10.1029/2020JB021567